Assessment of breast pathologies using nonlinear microscopy

Yuankai K. Tao[a], Dejun Shen[b,1], Yuri Sheikine[b,2], Osman O. Ahsen[a], Helen H. Wang[b], Daniel B. Schmolze[b], Nicole B. Johnson[b], Jeffrey S. Brooker[c], Alex E. Cable[d], James L. Connolly[b], and James G. Fujimoto[a,3]

[a]Department of Electrical Engineering and Computer Science and Research Laboratory of Electronics, Massachusetts Institute of Technology, Cambridge, MA 02139; [b]Department of Pathology, Beth Israel Deaconess Medical Center, Harvard Medical School, Boston, MA 02215; [c]Imaging Systems, Thorlabs, Inc., Sterling, VA 20166; and [d]Advanced Imaging Group, Thorlabs, Inc., Newton, NJ 07860

Rapid intraoperative assessment of breast excision specimens is clinically important because up to 40% of patients undergoing breast-conserving cancer surgery require reexcision for positive or close margins. We demonstrate nonlinear microscopy (NLM) for the assessment of benign and malignant breast pathologies in fresh surgical specimens. A total of 179 specimens from 50 patients was imaged with NLM using rapid extrinsic nuclear staining with acridine orange and intrinsic second harmonic contrast generation from collagen. Imaging was performed on fresh, intact specimens without the need for fixation, embedding, and sectioning required for conventional histopathology. A visualization method to aid pathological interpretation is presented that maps NLM contrast from two-photon fluorescence and second harmonic signals to features closely resembling histopathology using hematoxylin and eosin staining. Mosaicking is used to overcome trade-offs between resolution and field of view, enabling imaging of subcellular features over square-centimeter specimens. After NLM examination, specimens were processed for standard paraffin-embedded histology using a protocol that coregistered histological sections to NLM images for paired assessment. Blinded NLM reading by three pathologists achieved 95.4% sensitivity and 93.3% specificity, compared with paraffin-embedded histology, for identifying invasive cancer and ductal carcinoma in situ versus benign breast tissue. Interobserver agreement was $\kappa = 0.88$ for NLM and $\kappa = 0.89$ for histology. These results show that NLM achieves high diagnostic accuracy, can be rapidly performed on unfixed specimens, and is a promising method for intraoperative margin assessment.

nonlinear microscopy | breast cancer | pathology | imaging

Breast cancer is the most common cancer and cause of cancer-related death in women worldwide (1). In the United States, one in eight women will develop breast cancer in their lifetimes with an estimated 226,870 new cases and 39,510 deaths in 2012 (2). Breast-conserving therapy (BCT), lumpectomy followed by adjuvant radiation and/or chemotherapy and hormonal therapy, is a standard of care for early breast cancer and achieves survival and local recurrence rates comparable to mastectomy while providing superior cosmetic outcomes and reduced morbidity (3–5). Local recurrence rates are correlated with surgical margin status, which is evaluated using intraoperative examination and postoperative histopathology. However, there is no consensus on surgical margin widths, and differing conventions for negative and close margins have shown inconsistent correlations with therapeutic outcomes (6–9). Despite these inconsistencies, margins initially positive for invasive cancer or ductal carcinoma in situ (DCIS) almost always require surgical reexcision (92.6% when positive for DCIS and 83.5% when positive for invasive cancer) (9), and up to 40% of all women undergoing BCT require repeat surgeries from positive or close margins (10–12). In addition to surgical complications and increased patient anxiety, repeat surgeries increase healthcare costs (13).

Surgical margins are assessed based on the distance between tumor cells and inked surfaces of lumpectomy specimens using either postoperative paraffin-embedded hematoxylin and eosin (H&E) histology or intraoperative frozen-section analysis (FSA). Paraffin-embedded histology is the gold standard but requires long fixation and processing times (~16 h) and has limited sampling area. FSA offers faster processing times (~20 min per section), which enables intraoperative feedback and can potentially reduce repeat surgeries (14). However, FSA requires increased surgical time and has reduced accuracy compared with paraffin-embedded histology (15–19). FSA studies have reported sensitivities between 65% and 91% and specificities between 85% and 100% (16, 17, 20–23), and false-negative rates as high as 36% for small (<1 cm) or nonpalpable lesions, such as DCIS (24). FSA is particularly difficult in fatty breast specimens, and freezing artifacts make subsequent diagnosis on paraffin-embedded sections more difficult (25, 26). Moreover, FSA has limited sampling because it requires serial processing of each specimen. Therefore, there is a clinical need for improved methods to assess breast cancer surgical margins in real time.

Reflectance confocal microscopy has been compared with standard histology in human breast core needle biopsy specimens

---

Significance

Development of methods for rapid intraoperative assessment of breast pathologies is important for decreasing the rate of surgical reexcisions during breast-conserving therapy. Frozen-section analysis is the most widely used method for intraoperative margin assessment but is time consuming, has limited diagnostic accuracy, and produces freezing artifacts. This manuscript demonstrates nonlinear microscopy for rapid assessment of surgical breast specimens without need for fixation, embedding, and sectioning required for conventional histology. Blinded reading of nonlinear microscopy images by three pathologists achieved 95.4% sensitivity, 93.3% specificity, and 94.1% overall accuracy compared with histology for identifying invasive cancer and ductal carcinoma in situ versus benign breast tissue. The results suggest that nonlinear microscopy is a promising method for intraoperative assessment of breast surgical excision specimens.

---

and mouse mammary glands (27, 28). Similarly, fluorescence confocal studies demonstrated rapid imaging of excised tissue surfaces but did not evaluate correspondence with histological diagnoses (29). Optical coherence tomography (OCT) and optical coherence microscopy (OCM) provide depth-resolved imaging using backscattered light (30). Early OCT studies investigated ex vivo breast pathologies and correspondence with histology (31, 32). Zhou et al. (33) correlated OCT and *en face* OCM images with corresponding histology in 44 ex vivo human breast specimens, but did not assess diagnostic sensitivity or specificity. Nguyen et al. (34) performed OCT imaging on breast specimens from 37 patients and demonstrated 100% sensitivity and 82% specificity for detecting positive or close margins compared with histology, using a 17-specimen training set and 20-specimen study set. Assayag et al. (35) performed the most comprehensive study to date, conducting a blinded reading of 75 specimens from 22 patients using full-field *en face* OCT with corresponding histology. Reading by two pathologists yielded 94% and 90% sensitivity and 75% and 79% specificity, respectively, for detecting benign vs. cancer pathology. These results are promising, but because OCT has limited nuclear contrast, image interpretation uses different features than those in standard histology. Significant training is required for accurate interpretation and specificities have been limited.

Nonlinear (multiphoton, two-photon, and harmonic generation) microscopy (NLM), developed by Denk, Strickler, and Webb (36) in 1990, enables high-resolution imaging in optically scattering tissues, providing a powerful alternative to OCT and OCM. NLM has reduced imaging depth compared with OCT and OCM, but improved depths over fluorescence and confocal microscopy (37, 38). The ability to use both intrinsic and extrinsic contrast in NLM enables visualizing nuclear size and shape, and morphological changes, such as reorganization of collagen, associated with breast cancer (39–41). An early study by Zipfel et al. (42) suggested the potential of NLM for imaging intact tissue, demonstrating in vivo imaging with intrinsic two-photon fluorescence (TPF) and second harmonic generation (SHG) contrast in mice. However, to our knowledge, there are no previous studies assessing the diagnostic performance of NLM in human breast pathologies.

In this manuscript, we demonstrate NLM assessment of breast pathologies in fresh, unfixed surgical specimens. A rapid staining, nuclear-bound extrinsic fluorophore combined with intrinsic contrast from stromal collagen allows direct visualization of features analogous to those in paraffin-embedded histology. Clinical pathology interpretation is facilitated by mapping TPF and SHG NLM contrast channels to display structures and colors analogous to H&E staining. We overcome the limited field of view (FOV) in high-magnification imaging using a combination of scanning and field mosaicking, enabling subcellular resolution over square-centimeter specimens. Blinded reading of NLM images by three breast pathologists achieved 95.4% sensitivity and 93.3% specificity, compared with histology, for identifying invasive cancer and DCIS vs. benign breast tissue. These results suggest the utility of NLM for real-time assessment of breast cancer surgical margin status.

Results

A prospective study with 179 surgical specimens from 50 patients was performed to evaluate the diagnostic accuracy of NLM compared with paraffin-embedded histology. NLM images were acquired from freshly excised, unfixed human breast tissue specimens. Specimens were stained with acridine orange (AO) for TPF nuclear contrast and intrinsic SHG from collagen was used as a second channel. To facilitate image interpretation and histopathological diagnosis, NLM detection channels were mapped into pseudo-H&E colors (Fig. 1) with the TPF nuclear and SHG collagen channels displayed as a blue stain and pink counterstain, respectively (*Materials and Methods*). Examples of NLM

images and corresponding paraffin-embedded histology of normal breast tissue, DCIS, and invasive ductal carcinoma (IDC) are shown. Additional examples of fibroadenoma and invasive lobular carcinoma (ILC) are in Fig. S1.

Normal Breast Tissue. Breast parenchyma consists of lobes, separated by fibro-adipose stroma, that branch into successively smaller ducts, ductules, and terminal ductules (acini). These acini are grouped into lobules called terminal duct lobular units (TDLUs). Fig. 2 shows a 6 × 6.25-mm NLM image and corresponding paraffin-embedded histology of a normal breast specimen. The NLM dataset consisted of eight depth sections acquired at 25-μm increments from the tissue surface and sampled at 600-megapixel native resolution. NLM shows cross-sections of acini lined by a two-cell layer epithelium supported by a basement membrane (Fig. 2, red box). Normal fibro-adipose stroma is seen with adipocytes consisting of nuclei flattened at the periphery of large lipid droplets (Fig. 2, green box) and fibrocollagenous stroma generating a strong SHG background (Fig. 2, blue box). An enlargement of this figure is in Fig. S2.

DCIS. DCIS is a preinvasive accumulation of neoplastic ductal cells within the lumens of mammary ducts and lobules, present in most invasive breast cancers, and a likely precursor to invasive carcinoma. DCIS is heterogeneous, and the likelihood of progression to invasive breast cancer and recurrence is associated with subtype and grade. Diagnostic criteria for DCIS includes low, intermediate, and high grade, which are distinguished by the presence of increasingly irregular nuclei, and architectural types, including cribriform, micropapillary, solid, or solid with central or comedo necrosis (necrotic tumor cell debris inside ducts). NLM achieves sufficient resolution to identify nuclear and architectural features enabling real-time histopathological assessment of DCIS type and grade. Fig. 3 shows an 8.25 × 5-mm NLM image and corresponding paraffin-embedded histology with examples of DCIS subtypes. The NLM dataset consisted of six depth sections acquired at 10-μm increments from the tissue surface and each sampled at 660-megapixel native resolution. NLM shows dilated ducts lined by monotonous cells with finger-like protuberances in the lumen, indicative of micropapillary growth (Fig. 3, red box). Micropapillary DCIS is a subtype that may be more widespread and underestimated by mammography and, therefore, is a known risk factor for local recurrence after BCT. NLM also shows comedo necrosis (Fig. 3, green box), which indicates high-grade DCIS and is a predictor of recurrence. The duct lumen is filled with a central area of necrotic debris and surrounded by large pleomorphic cells with prominent nucleoli (Fig. 3, blue box). An enlargement of this figure is in Fig. S3.

Invasive Carcinoma. In BCT, primary lesions commonly consist of invasive ductal or lobular carcinoma, accounting for 80% and 15% of all lesions, respectively. Although identifiable on gross surgical examination, invasive carcinomas are often accompanied by nonpalpable, in situ lesions. Breast carcinoma is classified as invasive once it leaves the confines of a duct and cells are present in the stroma. There may be variable gland formation or a linear pattern of invading cells and a wide range of cytologic atypia. Fig. 4 shows a 18.25 × 12-mm region with both DCIS and IDC. The NLM data consisted of eight depth sections acquired at 15-μm increments from the tissue surface, each sampled at 3.5-gigapixel native resolution. NLM shows distinct regions of DCIS and IDC (*Right*) and benign breast tissue (*Left*). The intraductal sieve-like features are associated with cribriform DCIS, indicative of a low- to intermediate-grade lesion, characterized by dilated ducts filled with monotonous cells (cells within lesions that are histologically similar) and fenestrations (open spaces within ducts/lobules involved by DCIS) (Fig. 4, red box). IDC is adjacent to DCIS and exhibits neoplastic cells infiltrating

www.manaraa.com
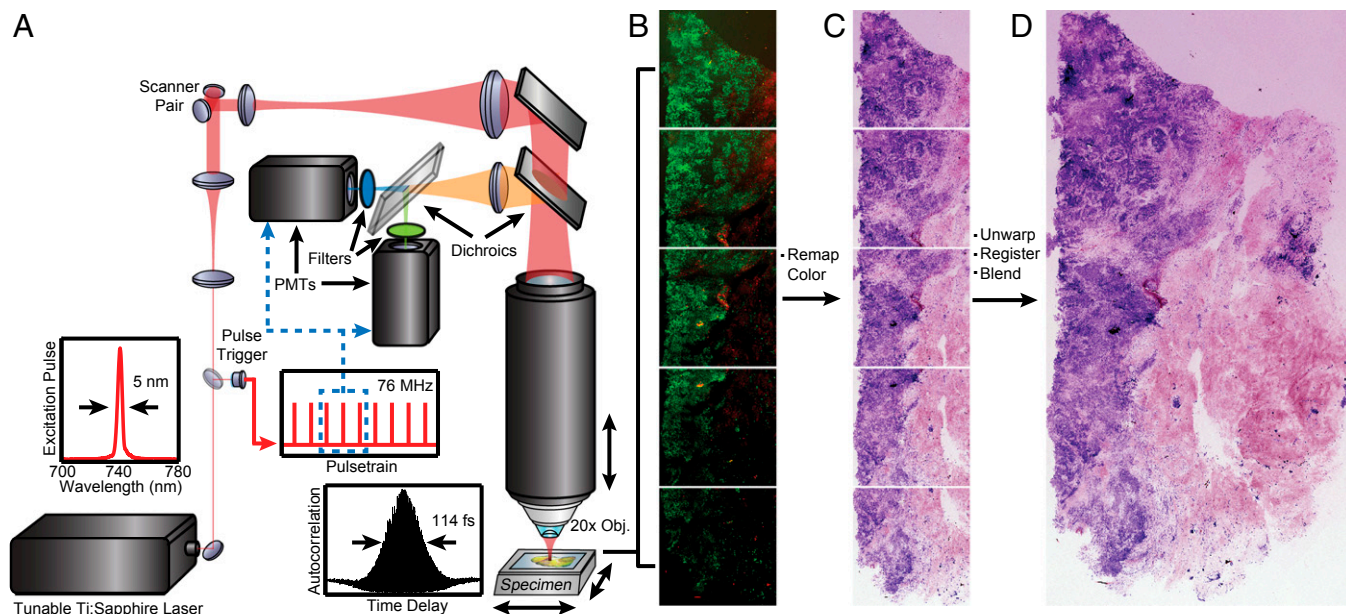
Fig. 1. Schematic of extended FOV nonlinear microscopy. (*A*) Dual detection channels collect TPF and SHG signals for nuclear and stromal contrast, respectively. High-magnification fields were imaged using a 20×, 0.95 N.A. objective with a 480 × 480-μm field sampled with 1,024 × 1,024 pixels at 19 frames per s. (*B*) Overlapping fields are automatically acquired using a motorized stage translating the specimen in a serpentine pattern and serial depth sections obtained by motorized translation of the optics. (*C*) Field distortion correction, pseudo-H&E color remapping, and (*D*) image mosaicking are applied in postprocessing.

surrounding breast stroma (Fig. 4, green box). In the benign region, NLM shows areas of intraductal alterations consistent with columnar cell change (Fig. 4, blue box). Here, native epithelial cells are replaced by columnar cells, associated with flat epithelial atypia, atypical ductal hyperplasia, low-grade DCIS, and lobular neoplasia. NLM also shows loss of SHG signal, particularly in areas of IDC, which may result from collagen reorganization and extracellular matrix remodeling known to accompany tumorigenesis (desmoplastic stromal response). Examples of invasive lobular carcinoma were also identified on NLM (Fig. S4). Here, uniform invasive lobular carcinoma cells are shown infiltrating the stroma and arranged in slender linear strands. Magnified regions show nuclear pleomorphism with varying nuclear size and shape (Fig. S4 *A* and *B*). Another example of invasive tumor shows carcinoma with mixed ductal and lobular features (Fig. S4 *C* and *D*). Invasive lobular carcinoma cells infiltrate adjacent adipocytes and mimic the appearance of fat necrosis. A region of IDC can also be identified with cells arranged in small tubules, cords, and nests. An enlargement of this figure is in Fig. S4.

Sensitivity and Specificity for NLM Diagnosis of Breast Pathologies. Surgical margin assessment requires high sensitivity and specificity to differentiate malignant pathologies (invasive cancer and DCIS) vs. benign breast tissue. However, pathology subtypes were also assessed to identify how they contribute to overall sensitivity and specificity. A double-blinded histopathological assessment of NLM images and corresponding paraffin-embedded H&E sections was performed by three pathologists. After reviewing a 30-specimen training set of paired NLM and H&E images, each pathologist diagnosed 138 NLM images while blinded to corresponding H&E. Subtypes assessed included the following: normal breast tissue, fibroadenoma (Fig. S5), usual ductal hyperplasia, fibrocystic changes (including biopsy site changes), lobular carcinoma in situ (LCIS), DCIS, IDC, and ILC. Similar pathology subtypes were grouped during data analysis to determine NLM diagnostic accuracy for detecting benign and malignant tissues (Fig. S6). The combined results of the three blinded NLM

readings achieved an average 95.4% (95% confidence interval, 90.3–98.0) sensitivity and 93.3% (95% confidence interval, 89.3–95.9) specificity for distinguishing benign tissue vs. invasive cancer and DCIS compared with corresponding H&E diagnoses. Invasive cancer and DCIS were grouped together because these pathology subtypes determine the need for surgical reexcision. The negative predictive value was 97.1% and accuracy was 94.1%. Interobserver agreement between the three pathologists was almost perfect (43) for both NLM and H&E with κ = 0.88 and κ = 0.89, respectively (Table 1). The reading times for NLM and
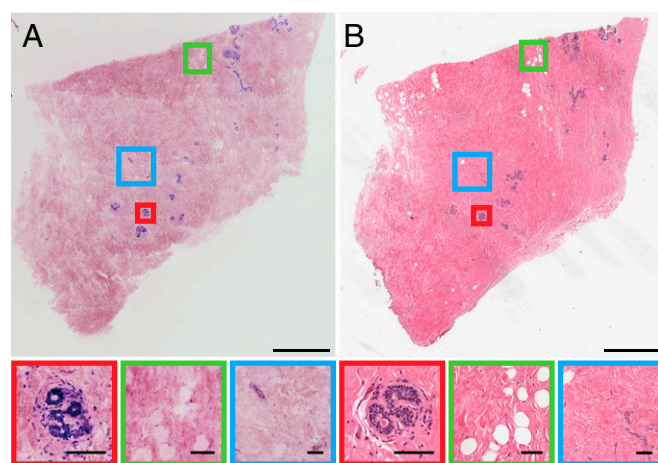
Fig. 2. Normal human breast tissue imaged using NLM. (*A*) NLM and (*B*) corresponding paraffin-embedded H&E histology. (Scale bar: 1 mm.) Magnified regions show a TDLU (red box) (scale bar: 150 μm), adipocytes (green box) (scale bar: 150 μm), and fibrocollagenous stroma (blue box) (scale bar: 150 μm). Image shows maximum-intensity projection through eight depth sections acquired at 25-μm increments from the tissue surface. FOV: 6 × 6.25 mm (600 megapixels). NLM data: tinyurl.com/a3qgzco. H&E data: tinyurl.com/ajdwe8d.

Tao et al.

www.manaraa.com
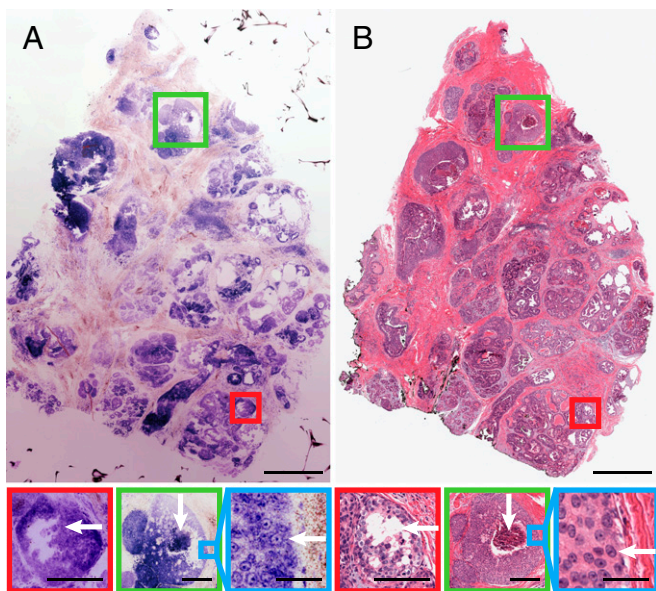
Fig. 3. Human breast specimen with DCIS in various histologic patterns. (*A*) NLM and (*B*) corresponding paraffin-embedded histology showing different DCIS subtypes. (Scale bar: 1 mm.) Finger-like projections of neoplastic cells invading the duct lumen are indicative of micropapillary DCIS (red box). (Scale bar: 250 μm.) Irregular-shaped cavities with cellular debris and comedo plug are indicative of comedo DCIS (green box). (Scale bar: 250 μm.) Individual cell nuclei at the periphery of the comedo DCIS exhibit prominent nucleoli consistent with high-grade DCIS (blue box). (Scale bar: 50 μm.) Image shows maximum-intensity projection through six depth sections acquired at 10-μm increments from the tissue surface. FOV: 8.25 × 5 mm (660 megapixels). NLM data: tinyurl.com/cwyly6s. H&E data: tinyurl.com/9teff9a.

H&E data were not statistically significantly different, 191 min (mean of 1.38 min per specimen) for NLM and 157 min (mean of 1.14 min per specimen) for H&E with $P = 0.31$.

Discussion

Our results demonstrate NLM can differentiate benign from malignant breast pathologies with accuracies comparable to paraffin-embedded H&E histology. This study also assessed common benign and malignant histopathological subtypes (Fig. S6). For subtypes, specimen numbers were insufficient to achieve statistical significance due to the rarity of some subtypes, but results suggest how subtypes and pathological features influenced NLM diagnostic sensitivity and specificity. Invasive carcinomas and DCIS were most easily diagnosed, whereas benign pathologies (usual ductal hyperplasia and fibrocystic changes) were more difficult. This finding may be expected because both DCIS and usual ductal hyperplasia are proliferative lesions; and fibrocystic changes, which include previous biopsy site changes, may present as reactive atypia. DCIS was often misdiagnosed as IDC; however, both are malignant subtypes and this does not affect overall sensitivity and specificity. It can be difficult to distinguish DCIS from IDC with a nest-like invasive pattern on H&E histology, and immunostains are often used in this situation. Subtype results also showed that LCIS was difficult to diagnose using NLM. Misclassifications of LCIS may be attributed to inconsistent visualization of subnuclear features and distended acini associated with LCIS. However, intraoperative assessment of specimen margin status does not require subtype identification, but only detection of DCIS or invasive carcinoma. Although usual ductal hyperplasia, fibrocystic changes, and LCIS were difficult to identify using NLM, the detection of these pathologies at surgical margins would not clinically alter surgical procedure. Furthermore, NLM was read without knowledge of clinical history or biopsy findings, whereas in

an actual clinical surgical scenario, diagnoses from core needle biopsies would be available a priori and NLM would not be used to make de novo diagnoses. This a priori information is expected to further enhance diagnostic accuracy.

The 95.4% sensitivity and 93.3% specificity of NLM is higher sensitivity than FSA, and similar sensitivity, but higher specificity than OCT. FSA has sensitivities from 65% to 91% and specificities from 85% to 100% (16, 17, 20–23). OCT images up to 2 mm below the tissue surface, and a previous breast surgical specimen imaging study demonstrated 100% sensitivity and 82% specificity in a 20-specimen study set (34). However, nuclei were not visualized, diagnoses were made using image features different from standard H&E, and pathology subtyping was not performed. A larger *en face* OCT study demonstrated full-field imaging of centimeter specimens with 150- to 200-μm imaging depth. Blinded reads by two pathologists of 75 specimens from 22 patients yielded 94% and 90% sensitivity and 75% and 79% specificity, respectively, for detecting cancer compared with histology (35). Pathology subtyping was not performed, but IDC, DCIS, and fibroadenoma were reported to be more readily identified than other pathologies. Our NLM study has the best diagnostic accuracy and is the largest to date, reporting confidence intervals, interreader agreement, and pathology subtyping. Compared with OCT, NLM has advantages of ease of interpretation with minimal training because NLM images display features analogous to those visualized in H&E staining using an analogous color map.

NLM has higher sensitivity than FSA and should improve sampling of the surgical margin. Possible methods for using NLM are discussed in *Possible Examination Protocols*. Recent studies evaluated intraoperative touch imprint cytology and FSA vs.
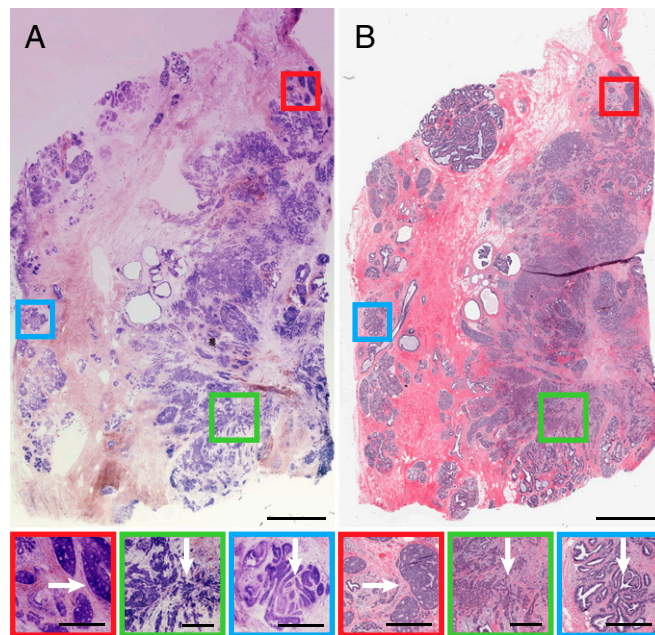
Fig. 4. Human breast specimen with regions of DCIS and IDC adjacent to normal tissue. (*A*) NLM and (*B*) corresponding paraffin-embedded histology showing DCIS and IDC (*Right*) vs. benign breast tissue (*Left*). (Scale bar: 2 mm.) Sieve-like appearance is associated with cribriform DCIS, consistent with low- to intermediate-grade DCIS (red box). (Scale bar: 500 μm.) IDC region shows neoplastic cells infiltrating breast stroma (green box). (Scale bar: 500 μm.) Magnified view of abnormal cellular regions show features consistent with columnar cell change (blue box). (Scale bar: 500 μm.) Image shows maximum-intensity projection through eight depth sections acquired at 15-μm increments from the tissue surface. FOV: 18.25 × 12 mm (3.5 gigapixels). NLM data: tinyurl.com/ccueff3. H&E data: tinyurl.com/cnvp8yy.

Tao et al.

Table 1. Sensitivity and specificity of NLM for differentiating benign breast tissue and DCIS/IDC/ILC

Benign vs. DCIS/IDC/ILC		95% Confidence	
		Lower limit	Upper limit
Sensitivity, %	95.4	90.3	98.0
Specificity, %	93.3	89.3	95.9
Accuracy, %	94.1		
PPV, %	89.4		
NPV, %	97.1		

paraffin-embedded sections for evaluating breast surgical specimen margins and the rates of subsequent reexcision (44, 45). In these studies, intraoperative margin assessment decreased reexcision rates from ~35% (i.e., postoperative paraffin-embedded section assessment) to ~10–11% (i.e., intraoperative assessment). These studies did not specify the fraction of the margin examined using intraoperative FSA, but examination of one to two sections is standard. Even limited sampling of the margin may substantially reduce healthcare costs, as indicated in a study where intraoperative assessment reduced total surgical costs from $22,013 ± $13,821 to $15,341 ± $4,328 (46).

Image mosaicking was used to acquire NLM images over large FOVs for coregistration with paraffin-embedded histology. Mosaicking was not optimized for speed, and a standard commercial nonlinear microscope was used. These factors contributed to a low NLM imaging speed (*Imaging Speed*), and we are currently redesigning the microscope to increase FOV and imaging speed. Mosaicking would not be required to image breadloafed specimens and current imaging speeds are sufficient. The feasibility of imaging the entire specimen surface would ultimately depend on NLM imaging speed and specimen size, because surface areas can be many square centimeters for larger specimens.

In practice, intraoperative NLM diagnoses would be confirmed using postoperative paraffin-embedded histology. Our NLM nuclear stain (AO) cationically intercalates nucleic acids and might interfere with histological stains or immunostaining protocols. Our results showed no interference with standard paraffin-embedded H&E staining and no nuclear fluorescence in paraffin-embedded tissue blocks, indicating that acridine staining would not confound fluorescence-based immunohistochemistry techniques such as fluorescence in situ hybridization. A preliminary test using AO-stained tissue for estrogen and progesterone receptor immunohistochemical assays showed no interference (Fig. S7). Additional tests using common immunostains and genetic assays are needed to show AO does not interfere with standard breast cancer assays. It is important to note that nuclear staining of surgical specimens would generally not interfere with molecular and genetic assays because these markers are assessed on core needle biopsy before surgery. Furthermore, NLM would not preclude repeat immunostaining and genetic testing of surgical specimens because acridine only penetrates ~300 μm into the specimen (*Assessing Effects of AO Staining*), and only exposed specimen surfaces would be stained. This is an important consideration for medical centers archiving surgical specimens for tumor banks.

In conclusion, we report an NLM technology and methodology for imaging unfixed surgical breast specimens. To our knowledge, this is the first study to assess NLM diagnostic performance for breast cancer pathologies. Blinded NLM readings by three pathologists achieved an average 95.4% sensitivity and 93.3% specificity for distinguishing benign tissue vs. invasive cancer and DCIS compared with corresponding H&E diagnoses. Interobserver agreement between the three pathologists for NLM and conventional histology was κ = 0.88 and κ = 0.89, respectively.

NLM can potentially overcome sampling limitations associated with standard paraffin-embedded histology or FSA. The ability of NLM to image in real time, without the need for histological processing, should enable intraoperative assessment. Finally, NLM is nondestructive and subsequent histopathological diagnoses would not be confounded by freezing artifacts common in FSA. These combined advantages suggest that NLM can be a powerful tool for real-time intraoperative assessment of breast cancer surgical specimens and may reduce the rate of repeat surgeries from close or positive margins. In addition, NLM may also be applicable for lung, thyroid, as well as head and neck surgeries requiring real-time assessment of surgical specimens.

Materials and Methods

Tissue Preparation. Studies were performed under protocols approved by the Massachusetts Institute of Technology Committee on the Use of Humans as Experimental Subjects and Beth Israel Deaconess Medical Center Committee on Clinical Investigations and Institutional Review Board. Informed consent was not required because imaging was limited to discarded human tissues deidentified of protected health information. Fresh unfixed surgical specimens not required for clinical diagnosis were stored in refrigerated DMEM for less than 4 h before imaging. The tissue was grossed and trimmed to remove extraneous fat and expose breast parenchyma. Specimens were stained with 75 μM AO buffered in DMEM (30 s) and washed in fresh DMEM (30 s). The specimens were held in histology-processing cassettes fitted with a microscope coverslip to provide a flat optical surface for NLM. This enabled the specimen to be imaged and fixed without disturbing the surface. After NLM, specimens were fixed in 10% (vol/vol) neutral buffered formalin for a minimum of 24 h before processing, embedding, sectioning, and staining. Histological sectioning was performed parallel to the specimen surface to match the NLM imaging plane.

Large-Field NLM Image Acquisition. NLM was performed using a ~100-fs tunable Ti:sapphire laser (Mira Optima 900-F; Coherent) at ~740 nm with a 76-MHz repetition rate and a commercial nonlinear microscope (Thorlabs). The laser beam was scanned with a 7.9-kHz resonant and galvanometric scanner for fast- and slow-axis raster scanning, respectively. Dual-channel photomultipliers (H7422; Hamamatsu) were used to collect nuclear-bound TPF from AO and intrinsic collagen SHG. Signals were separated using 530 ± 25- and 370 ± 25-nm fluorescence filter cubes. Images were acquired using <20-mW power on the sample. High-magnification fields were imaged using a 20×, 0.95 N.A. objective (XLUMPFL20XW; Olympus) with a 480 × 480-μm field with 0.44 × 0.44 × 1.21-μm (x, y, z) resolution sampled with 1,024 pixels × 1,024 pixels at 19 frames per s.

Image Mosaicking and Postprocessing. Specimens were automatically scanned with a serpentine pattern using a high-precision linear stage with 250-nm repeatability (MLS203; Thorlabs). Serial depth sections were automatically acquired by motorized translation of the optics. Multiple depth images were acquired to ensure the entire specimen surface was imaged in case a small specimen tilt caused a depth shift. Adjacent mosaic tiles were acquired with a 50% overlap to remove any edge artifacts during digital mosaicking and improve signal-to-noise by averaging. Field aberrations in each image tile were corrected in post-processing prior to mosaicking (Fig. S8). To overcome the limitations of commercial image viewers for gigapixel-sized datasets, stitched NLM images were converted to a hierarchal image format (Fig. S9, Deep Zoom; Microsoft) similar to Google Maps (*Deep Zoom*).

Histological Assessment and Reading Protocol. Embedded histological blocks were cut into 5-μm–thick sections at 10-μm steps over the imaging range of the corresponding NLM dataset to enable matching sections. Corresponding paraffin-embedded H&E sections were scanned at 20× magnification (Aperio) and converted to Deep Zoom datasets for visualization and assessment. Eleven datasets from the 179 specimens were discarded for poor depth mismatch between the NLM images and corresponding paraffin-embedded H&E depth sections. These data were from specimens that were inadequately flattened during embedding, causing an uneven surface during microtoming. The remaining datasets were divided into a 30-specimen training set and 138 reading set that included paired NLM and H&E images.

Three pathologists were trained on 30 paired NLM and H&E data and asked to identify histopathological subtypes on 138 randomized NLM images while blinded to the corresponding H&E sections. For each NLM dataset, pathologists were first presented with a maximum-intensity projection of all depth sections as a global overview of the specimen. This was particularly useful in tilted

www.manaraa.com

specimens where individual depth sections were varying relative to the tissue surface. The visualization and reading software allowed the pathologist to pan and zoom a region of interest and step through the depth sections in the NLM dataset for a given FOV. The final diagnoses for each NLM dataset were made using an individual depth section to avoid potential artifacts from the maximum-intensity image. Randomized corresponding H&E images were assessed 1 wk later to reduce memory confounders. H&E diagnoses were made on a single section, and NLM diagnoses were made based on several images acquired at depths spanning the H&E sectioning depth.

Statistical Analysis. NLM and corresponding H&E results were compared on a per-specimen basis for each pathologist reader. In addition to assessing individual histopathological subtypes, the subtypes were also grouped into benign, malignant, in situ, invasive, ductal, and lobular categories. Sensitivity, specificity, accuracy, positive predictive value, negative predictive value, and 95% confidence intervals were calculated for each grouping for each individual pathologist, and results from all three pathologists were combined. Interobserver variability for histopathological diagnoses using NLM and standard H&E was compared by calculating the Fleiss' κ.

1. American Cancer Society (2011) *Global Cancer Facts & Figures* (American Cancer Society, Atlanta), 2nd Ed.
2. American Cancer Society (2012) *Cancer Facts & Figures 2012* (American Cancer Society, Atlanta).
3. Fisher B, et al. (1989) Eight-year results of a randomized clinical trial comparing total mastectomy and lumpectomy with or without irradiation in the treatment of breast cancer. *N Engl J Med* 320(13):822–828.
4. Fisher B, et al. (1995) Reanalysis and results after 12 years of follow-up in a randomized clinical trial comparing total mastectomy with lumpectomy with or without irradiation in the treatment of breast cancer. *N Engl J Med* 333(22):1456–1461.
5. Nesvold IL, Dahl AA, Løkkevik E, Marit Mengshoel A, Fosså SD (2008) Arm and shoulder morbidity in breast cancer patients after breast-conserving therapy versus mastectomy. *Acta Oncol* 47(5):835–842.
6. von Smitten K (2008) Margin status after breast-conserving treatment of breast cancer: How much free margin is enough? *J Surg Oncol* 98(8):585–587.
7. Dunne C, Burke JP, Morrow M, Kell MR (2009) Effect of margin status on local recurrence after breast conservation and radiation therapy for ductal carcinoma in situ. *J Clin Oncol* 27(10):1615–1620.
8. Pleijhuis RG, et al. (2009) Obtaining adequate surgical margins in breast-conserving therapy for patients with early-stage breast cancer: Current modalities and future directions. *Ann Surg Oncol* 16(10):2717–2730.
9. McCahill LE, et al. (2012) Variability in reexcision following breast conservation surgery. *JAMA* 307(5):467–475.
10. Sabel MS, et al. (2009) Residual disease after re-excision lumpectomy for close margins. *J Surg Oncol* 99(2):99–103.
11. Morrow M, et al. (2009) Surgeon recommendations and receipt of mastectomy for treatment of breast cancer. *JAMA* 302(14):1551–1556.
12. Kobbermann A, et al. (2011) Impact of routine cavity shave margins on breast cancer re-excision rates. *Ann Surg Oncol* 18(5):1349–1355.
13. Osborn JB, Keeney GL, Jakub JW, Degnim AC, Boughey JC (2011) Cost-effectiveness analysis of routine frozen-section analysis of breast margins compared with reoperation for positive margins. *Ann Surg Oncol* 18(11):3204–3209.
14. Bancroft JD, Stevens A (2008) *Theory and Practice of Histological Techniques* (Churchill Livingstone, Edinburgh), 6th Ed.
15. Weiser MR, et al. (2000) Is routine intraoperative frozen-section examination of sentinel lymph nodes in breast cancer worthwhile? *Ann Surg Oncol* 7(9):651–655.
16. Cendán JC, Coco D, Copeland EM, 3rd (2005) Accuracy of intraoperative frozen-section analysis of breast cancer lumpectomy-bed margins. *J Am Coll Surg* 201(2):194–198.
17. Olson TP, Harter J, Muñoz A, Mahvi DM, Breslin T (2007) Frozen section analysis for intraoperative margin assessment during breast-conserving surgery results in low rates of re-excision and local recurrence. *Ann Surg Oncol* 14(10):2953–2960.
18. Layfield DM, Agrawal A, Roche H, Cutress RI (2011) Intraoperative assessment of sentinel lymph nodes in breast cancer. *Br J Surg* 98(1):4–17.
19. Liu LC, et al. (2011) Intraoperative frozen section analysis of sentinel lymph nodes in breast cancer patients: A meta-analysis and single-institution experience. *Cancer* 117(2):250–258.
20. Cabioglu N, et al. (2007) Role for intraoperative margin assessment in patients undergoing breast-conserving surgery. *Ann Surg Oncol* 14(4):1458–1471.
21. Fukamachi K, et al. (2010) Total-circumference intraoperative frozen section analysis reduces margin-positive rate in breast-conservation surgery. *Jpn J Clin Oncol* 40(6):513–520.
22. Sauter ER, et al. (1994) Is frozen section analysis of reexcision lumpectomy margins worthwhile? Margin analysis in breast reexcisions. *Cancer* 73(10):2607–2612.
23. Weber S, Storm FK, Stitt J, Mahvi DM (1997) The role of frozen section analysis of margins during breast conservation surgery. *Cancer J Sci Am* 3(5):273–277.
24. Cheng L, Al-Kaisi NK, Liu AY, Gordon NH (1997) The results of intraoperative consultations in 181 ductal carcinomas in situ of the breast. *Cancer* 80(1):75–79.
25. Ferreiro JA, Gisvold JJ, Bostwick DG (1995) Accuracy of frozen-section diagnosis of mammographically directed breast biopsies. Results of 1,490 consecutive cases. *Am J Surg Pathol* 19(11):1267–1271.
26. Menes TS, Tartter PI, Mizrachi H, Smith SR, Estabrook A (2003) Touch preparation or frozen section for intraoperative detection of sentinel lymph node metastases from breast cancer. *Ann Surg Oncol* 10(10):1166–1170.
27. Tilli MT, et al. (2007) Real-time imaging and characterization of human breast tissue by reflectance confocal microscopy. *J Biomed Opt* 12(5):051901.
28. Schiffhauer LM, et al. (2009) Confocal microscopy of unfixed breast needle core biopsies: A comparison to fixed and stained sections. *BMC Cancer* 9:265.
29. Abeytunge S, et al. (2013) Confocal microscopy with strip mosaicing for rapid imaging over large areas of excised tissue. *J Biomed Opt* 18(6):61227.
30. Huang D, et al. (1991) Optical coherence tomography. *Science* 254(5035):1178–1181.
31. Boppart SA, Luo W, Marks DL, Singletary KW (2004) Optical coherence tomography: Feasibility for basic research and image-guided surgery of breast cancer. *Breast Cancer Res Treat* 84(2):85–97.
32. Hsiung PL, et al. (2007) Benign and malignant lesions in the human breast depicted with ultrahigh resolution and three-dimensional optical coherence tomography. *Radiology* 244(3):865–874.
33. Zhou C, et al. (2010) Integrated optical coherence tomography and microscopy for ex vivo multiscale evaluation of human breast tissues. *Cancer Res* 70(24):10071–10079.
34. Nguyen FT, et al. (2009) Intraoperative evaluation of breast tumor margins with optical coherence tomography. *Cancer Res* 69(22):8790–8796.
35. Assayag O, et al. (2014) Large field, high resolution full-field optical coherence tomography: A pre-clinical study of human breast tissue and cancer assessment. *Technol Cancer Res Treat* 13(5):455–468.
36. Denk W, Strickler JH, Webb WW (1990) Two-photon laser scanning fluorescence microscopy. *Science* 248(4951):73–76.
37. Zipfel WR, Williams RM, Webb WW (2003) Nonlinear magic: Multiphoton microscopy in the biosciences. *Nat Biotechnol* 21(11):1369–1377.
38. Helmchen F, Denk W (2005) Deep tissue two-photon microscopy. *Nat Methods* 2(12):932–940.
39. Schnitt SJ (2003) The diagnosis and management of pre-invasive breast disease: Flat epithelial atypia—classification, pathologic features and clinical significance. *Breast Cancer Res* 5(5):263–268.
40. Provenzano PP, et al. (2006) Collagen reorganization at the tumor-stromal interface facilitates local invasion. *BMC Med* 4(1):38.
41. Provenzano PP, et al. (2008) Collagen density promotes mammary tumor initiation and progression. *BMC Med* 6:11.
42. Zipfel WR, et al. (2003) Live tissue intrinsic emission microscopy using multiphoton-excited native fluorescence and second harmonic generation. *Proc Natl Acad Sci USA* 100(12):7075–7080.
43. Landis JR, Koch GG (1977) The measurement of observer agreement for categorical data. *Biometrics* 33(1):159–174.
44. Esbona K, Li Z, Wilke LG (2012) Intraoperative imprint cytology and frozen section pathology for margin assessment in breast conservation surgery: A systematic review. *Ann Surg Oncol* 19(10):3236–3245.
45. Butler-Henderson K, Lee AH, Price RI, Waring K (2014) Intraoperative assessment of margins in breast conserving therapy: A systematic review. *Breast* 23(2):112–119.
46. Uecker JM, Bui EH, Foulkrod KH, Sabra JP (2011) Intraoperative assessment of breast cancer specimens decreases cost and number of reoperations. *Am Surg* 77(3):342–344.

Tao et al.